

# A FLOATING NODE METHOD FOR THE MODELLING OF DISCONTINUITIES WITHIN A FINITE ELEMENT

S. T. Pinho<sup>1\*</sup>, B. Y. Chen<sup>1,2</sup>, N. V. De Carvalho<sup>3</sup>, P. M. Baiz<sup>1</sup> and T. E. Tay<sup>2</sup>

<sup>1</sup>Dept. of Aeronautics, South Kensington Campus, Imperial College London. SW7 2AZ, U.K.

<sup>2</sup>Dept. of Mech. Eng., Nat. Univ. of Singapore. 21 Lower Kent Ridge Road, Singapore 119077

<sup>3</sup>National Institute of Aerospace, NASA Langley Research Center, Hampton, USA

\* Corresponding author ([silvestre.pinho@imperial.ac.uk](mailto:silvestre.pinho@imperial.ac.uk))

**Keywords:** *phantom node method; multiple cracks; matrix crack; delamination; crack interaction*

## 1 Introduction

This paper focuses on the accurate numerical representation of complex networks of evolving discontinuities in solids, with particular emphasis on cracks. The limitation of the standard finite element method (FEM) in approximating discontinuous solutions has motivated the development of re-meshing [1], smeared crack models [2, 3], the eXtended Finite Element Method (XFEM) [4–6] and the Phantom Node Method (PNM) [7].

We propose a new method which has some similarities to the PNM, but crucially: (i) does not introduce an error on the crack geometry when mapping to natural coordinates; (ii) does not require numerical integration over *only part* of a domain; (iii) can incorporate weak discontinuities and cohesive cracks more readily; (iv) is ideally suited for the representation of multiple and complex networks of (weak, strong and cohesive) discontinuities; (v) leads to the same solution as a finite element mesh where the discontinuity is represented explicitly; and (vi) is conceptually simpler than the PNM.

## 2 Brief overview of the Phantom Node Method

### 2.1 Introduction

The static equilibrium of a body with volume  $\Omega$  under body forces with density  $\mathbf{f}$  (acting on  $\Omega$ ) and traction  $\mathbf{t}$  acting on the boundary  $\Gamma_\Omega$  can be expressed in the weak form as:

$$\int_{\Omega} \boldsymbol{\epsilon}^T(\mathbf{v}) \boldsymbol{\sigma}(\mathbf{u}) \, d\Omega = \int_{\Omega} \mathbf{v}^T \mathbf{f} \, d\Omega + \int_{\Gamma_\Omega} \mathbf{v}^T \mathbf{t} \, d\Gamma_\Omega \quad (1)$$

where  $\mathbf{u}$  is the displacement;  $\mathbf{v}$  is the test function;  $\boldsymbol{\epsilon}$  is the strain, related to  $\mathbf{u}$  through the differential operator relative to Cartesian coordinates  $\mathcal{L}_x$  as  $\boldsymbol{\epsilon} = \mathcal{L}_x(\mathbf{u})$ ; and  $\boldsymbol{\sigma}$  is the stress, related to the strains through Hook's law as  $\boldsymbol{\sigma} = \mathbf{D}\boldsymbol{\epsilon}$ , with  $\mathbf{D}$  being the constitutive tensor. In the PNM, Fig. 1a, each real node  $i$  (characterised by its nodal coordinates  $\mathbf{x}_i$  and degrees of freedom, DoF,  $\mathbf{q}_i$ ) is accompanied by a phantom node  $i'$  (with the same nodal coordinates  $\mathbf{x}_{i'}$ , i.e.  $\mathbf{x}_{i'} \equiv \mathbf{x}_i$ , and associated DoF  $\mathbf{q}_{i'}$ ; in general,  $\mathbf{q}_{i'} \neq \mathbf{q}_i$ ).

### 2.2 Without a discontinuity

If there is no discontinuity to be modelled by the element (e.g. before failure), the element is simply a standard finite element. The vector of nodal coordinates is given as  $\mathbf{x}_\Omega$ . In the case of Fig. 1a,

$$\mathbf{x}_\Omega^T = [\mathbf{x}_1, \mathbf{x}_2, \mathbf{x}_3, \mathbf{x}_4] = [\mathbf{x}_{1'}, \mathbf{x}_{2'}, \mathbf{x}_{3'}, \mathbf{x}_{4'}]. \quad (2)$$

The Jacobian of the transformation from physical ( $\mathbf{x}$ ) to natural ( $\boldsymbol{\xi}$ ) coordinates is:

$$\mathbf{J} = \frac{d\mathbf{x}}{d\boldsymbol{\xi}} = \frac{d\mathbf{N}}{d\boldsymbol{\xi}} \mathbf{x}_\Omega, \quad (3)$$

where  $\mathbf{N}$  is a standard matrix of shape functions. Assuming an isoparametric formulation, the displacement field  $\mathbf{u}$  is related to the *real* DoF  $\mathbf{q}$  through the same matrix  $\mathbf{N}$ , i.e.:

$$\mathbf{u} = \mathbf{N}\mathbf{q}. \quad (4)$$

In the case of Fig. 1a,  $\mathbf{q}^T = [\mathbf{q}_1, \mathbf{q}_2, \mathbf{q}_3, \mathbf{q}_4]$ . The strains can also be expressed in terms of the real DoF  $\mathbf{q}$  as:

$$\boldsymbol{\epsilon} = \mathcal{L}_x(\mathbf{u}) = \mathcal{L}_\xi(\mathbf{N}) \mathbf{J}^{-1} \mathbf{q} = \mathbf{B}\mathbf{q}, \quad (5)$$

with  $\mathbf{B} = \mathcal{L}_\xi(\mathbf{N}) \mathbf{J}^{-1}$ , leading to:

$$\mathbf{K} = \int_{\Xi} \mathbf{B}^T \mathbf{D} \mathbf{B} \det(\mathbf{J}) \, d\Xi, \quad (6)$$

where  $\Xi$  is the integration domain (in natural coordinates) corresponding to  $\Omega$  (in physical coordinates), and to the vector of nodal forces:

$$\mathbf{Q} = \int_{\Xi} \mathbf{N}^T \mathbf{f} \det(\mathbf{J}) \, d\Xi + \int_{\Gamma_{\Xi}} \mathbf{N}^T \mathbf{t} \det(\mathbf{J}) \, d\Gamma_{\Xi} \quad (7)$$

where  $\Gamma_{\Xi}$  is the boundary corresponding to  $\Gamma_{\Omega}$ . Equilibrium, Eq. 1, becomes then:

$$\mathbf{K}\mathbf{q} = \mathbf{Q}. \quad (8)$$

Eq. 8 involves only the real DoF; for completeness, the phantom DoF can be defined using constraint equations so that they coincide with the real DoF; otherwise, they can be removed from the system of equations during assembly.

### 2.3 With a discontinuity

A discontinuity in the element can be predicted through generic stress-based criteria or otherwise; § 3.7 delves in more detail into propagation models and criteria. Once a discontinuity is predicted, the points at which it crosses the element are defined (points 5 and 6 in Fig. 1a). In this case, the vector of nodal coordinates  $\mathbf{x}_{\Omega}$  is still given by Eq. 2, and the Jacobian  $\mathbf{J}$  is still given by Eq. 3. However, the element is split in two partitions  $\Omega_A$  and  $\Omega_B$ , as indicated in Fig. 1a, and the displacement  $\mathbf{u}$  is no longer related to the real DoF  $\mathbf{q}$  by Eq. 4. Instead, the displacements  $\mathbf{u}_A$  and  $\mathbf{u}_B$ , in partitions  $\Omega_A$  and  $\Omega_B$  respectively, are interpolated separately from the respective DoF:

$$\mathbf{u}_A = \mathbf{N}\mathbf{q}_A \quad \text{and} \quad \mathbf{u}_B = \mathbf{N}\mathbf{q}_B. \quad (9)$$

In the case of Fig. 1a,  $\mathbf{q}_A^T = [\mathbf{q}_{1'}, \mathbf{q}_{2'}, \mathbf{q}_3, \mathbf{q}_4]$  and  $\mathbf{q}_B^T = [\mathbf{q}_1, \mathbf{q}_2, \mathbf{q}_{3'}, \mathbf{q}_{4'}]$ . The strains then become:

$$\boldsymbol{\epsilon}_A = \mathcal{L}_{\mathbf{x}}(\mathbf{u}_A) = \mathcal{L}_{\xi}(\mathbf{N})\mathbf{J}^{-1}\mathbf{q}_A = \mathbf{B}\mathbf{q}_A \quad (10)$$

$$\boldsymbol{\epsilon}_B = \mathcal{L}_{\mathbf{x}}(\mathbf{u}_B) = \mathcal{L}_{\xi}(\mathbf{N})\mathbf{J}^{-1}\mathbf{q}_B = \mathbf{B}\mathbf{q}_B. \quad (11)$$

with  $\mathbf{B} = \mathcal{L}_{\xi}(\mathbf{N})\mathbf{J}^{-1}$ . Note that the  $\mathbf{B}$  matrix (Eqs. 10 and 11) is the same for both partitions  $\Omega_A$  and  $\Omega_B$ . The stiffness matrices for partitions  $\Omega_A$  and  $\Omega_B$  are obtained by integrating over the corresponding domain in the natural space, i.e.:

$$\begin{aligned} \mathbf{K}_A &= \int_{\Xi_A} \mathbf{B}^T \mathbf{D} \mathbf{B} \det(\mathbf{J}) \, d\Xi \\ \mathbf{K}_B &= \int_{\Xi_B} \mathbf{B}^T \mathbf{D} \mathbf{B} \det(\mathbf{J}) \, d\Xi. \end{aligned} \quad (12)$$

Note that the integrands for partitions  $\Omega_A$  and  $\Omega_B$  in Eq. 12 are the same; only the integration domains ( $\Xi_A$  and  $\Xi_B$ , respectively) are different. Similarly, the force vectors are:

$$\mathbf{Q}_A = \int_{\Xi_A} \mathbf{N}^T \mathbf{f} \det(\mathbf{J}) \, d\Xi + \int_{\Gamma_{\Xi_A}} \mathbf{N}^T \mathbf{t} \det(\mathbf{J}) \, d\Gamma_{\Xi} \quad \text{and} \quad (13)$$

$$\mathbf{Q}_B = \int_{\Xi_B} \mathbf{N}^T \mathbf{f} \det(\mathbf{J}) \, d\Xi + \int_{\Gamma_{\Xi_B}} \mathbf{N}^T \mathbf{t} \det(\mathbf{J}) \, d\Gamma_{\Xi}, \quad (14)$$

where again the integrands are the same for both partitions but the integration domains differ. Finally, from Eq. 1, the equations of equilibrium are:

$$\mathbf{K}_A \mathbf{q}_A = \mathbf{Q}_A \quad \text{and} \quad \mathbf{K}_B \mathbf{q}_B = \mathbf{Q}_B. \quad (15)$$

## 3 Floating Node Method

### 3.1 Overview of the approach

§ 2 shows that, in the PNM, phantom DoF do not need an associated position vector before the element is split (§ 2.2; in fact, before the element is split, the phantom nodes are also not needed, but their presence is convenient for implementation in existing FE codes). After the element is split, the nodal position associated with the phantom DoF is not the most suitable in terms of transformation to the natural coordinate system nor in terms of integration.

This observation forms the basis of the FNM, which we detail in this section. In the FNM, see Fig. 1b, each *real* node  $i$  is characterised by its nodal coordinates  $\mathbf{x}_i$  and associated DoF  $\mathbf{q}_i$ ; in addition, the element contains a suitable number of floating DoF without pre-defined associated nodal position vectors.

### 3.2 Without a discontinuity

If there is no discontinuity to be modelled by the element (e.g. before failure), the formulation is the same as in the standard FEM or the PNM.

### 3.3 With a discontinuity

Once a discontinuity in the element is predicted (see § 3.7), and thus the coordinates of the points which define the intersection between the discontinuity and the element defined, the element is split in two or more partitions. We will illustrate in detail firstly the most typical situation in which the element is split in two partitions,  $\Omega_A$  and  $\Omega_B$  (Fig. 1b).

Unlike in the PNM, we define a vector of nodal coordinates for each partition  $\Omega_A$  and  $\Omega_B$ ,  $\mathbf{x}_A$  and  $\mathbf{x}_B$  respectively. For the case in Fig. 1b, these would be (c.f. Eq. 2):

$$\mathbf{x}_{\Omega_A}^T = [\mathbf{x}_5, \mathbf{x}_6, \mathbf{x}_3, \mathbf{x}_4] \quad \text{and} \quad \mathbf{x}_{\Omega_B}^T = [\mathbf{x}_1, \mathbf{x}_2, \mathbf{x}_6, \mathbf{x}_5]. \quad (16)$$

This is possible because  $\mathbf{x}_5$  and  $\mathbf{x}_6$  can be directly obtained once the failure criterion is fulfilled and the discontinuity is defined. Each partition has then a separate Jacobian (c.f. Eq. 3),

$$\mathbf{J}_A = \frac{d\mathbf{x}}{d\xi} = \frac{d\mathbf{N}}{d\xi} \mathbf{x}_{\Omega_A} \quad \text{and} \quad \mathbf{J}_B = \frac{d\mathbf{x}}{d\xi} = \frac{d\mathbf{N}}{d\xi} \mathbf{x}_{\Omega_B}. \quad (17)$$

The displacements  $\mathbf{u}_A$  and  $\mathbf{u}_B$ , in partitions  $\Omega_A$  and  $\Omega_B$  respectively, are interpolated separately from the respective DoF. Assuming an isoparametric formulation,

$$\mathbf{u}_A = \mathbf{N}\mathbf{q}_A \quad \text{and} \quad \mathbf{u}_B = \mathbf{N}\mathbf{q}_B. \quad (18)$$

In the case of Fig. 1b, which represents a strong discontinuity,  $\mathbf{q}_A^T = [\mathbf{q}_5, \mathbf{q}_6, \mathbf{q}_3, \mathbf{q}_4]$  and  $\mathbf{q}_B^T = [\mathbf{q}_1, \mathbf{q}_2, \mathbf{q}_{6'}, \mathbf{q}_{5'}]$ . Note that there are four different sets of floating DoF:  $\mathbf{q}_5$  is different from  $\mathbf{q}_{5'}$  and  $\mathbf{q}_6$  is different from  $\mathbf{q}_{6'}$ . If, for instance, a weak discontinuity were to be modelled, only two sets of floating DoF would be included in the element, and the DoF with a prime would coincide with those without a prime.

The strains then become (c.f. Eqs. 10 and 11):

$$\boldsymbol{\epsilon}_A = \mathcal{L}_{\mathbf{x}}(\mathbf{u}_A) = \mathcal{L}_{\xi}(\mathbf{N}) \mathbf{J}_A^{-1} \mathbf{q}_A = \mathbf{B}_A \mathbf{q}_A \quad (19)$$

$$\boldsymbol{\epsilon}_B = \mathcal{L}_{\mathbf{x}}(\mathbf{u}_B) = \mathcal{L}_{\xi}(\mathbf{N}) \mathbf{J}_B^{-1} \mathbf{q}_B = \mathbf{B}_B \mathbf{q}_B \quad (20)$$

with  $\mathbf{B}_A = \mathcal{L}_{\xi}(\mathbf{N}) \mathbf{J}_A^{-1}$  and  $\mathbf{B}_B = \mathcal{L}_{\xi}(\mathbf{N}) \mathbf{J}_B^{-1}$ . The stiffness matrices for partitions  $\Omega_A$  and  $\Omega_B$  are (c.f. Eq. 12):

$$\begin{aligned} \mathbf{K}_A &= \int_{\Xi} \mathbf{B}_A^T \mathbf{D} \mathbf{B}_A \det(\mathbf{J}_A) d\Xi \\ \mathbf{K}_B &= \int_{\Xi} \mathbf{B}_B^T \mathbf{D} \mathbf{B}_B \det(\mathbf{J}_B) d\Xi \end{aligned} \quad (21)$$

Note that the integrands for partitions  $\Omega_A$  and  $\Omega_B$  in Eq. 21 are different but the integration domain ( $\Xi$ ) is the same (the usual integration domain of a standard finite element). Similarly, the force vectors are (c.f. Eqs. 13 and 14):

$$\begin{aligned} \mathbf{Q}_A &= \int_{\Xi} \mathbf{N}^T \mathbf{f} \det(\mathbf{J}_A) d\Xi + \int_{\Gamma_{\Xi}} \mathbf{N}^T \mathbf{t} \det(\mathbf{J}_A) d\Gamma_{\Xi} \\ \mathbf{Q}_B &= \int_{\Xi} \mathbf{N}^T \mathbf{f} \det(\mathbf{J}_B) d\Xi + \int_{\Gamma_{\Xi}} \mathbf{N}^T \mathbf{t} \det(\mathbf{J}_B) d\Gamma_{\Xi}. \end{aligned} \quad (22)$$

Finally, from Eq. 1, the equations of equilibrium are:

$$\mathbf{K}_A \mathbf{q}_A = \mathbf{Q}_A \quad \text{and} \quad \mathbf{K}_B \mathbf{q}_B = \mathbf{Q}_B. \quad (23)$$

### 3.4 Different geometries for the discontinuities and integration

Fig. 1b (see also Fig. 2a) shows one particular case for the intersection between a quadrilateral element and a strong discontinuity. Another possibility (needed also to represent accurately the crack tip, see § 3.6) is shown in Fig. 2b. Finally, other possibilities for the intersection may lead to different partitions of  $\Omega$  (Figs. 2c, 2d, 2e, 2f, 2g and 2h). Cohesive cracks (Fig. 2i) can be represented by partitioning the integration domain  $\Omega$  into two quadrilaterals ( $\Omega_A$  and  $\Omega_B$ ) and a surface ( $\Gamma_{\Omega_c}$ ).

### 3.5 Representation of discontinuities

Representing a discontinuity across an entire mesh implies passing information which defines this discontinuity to each element. With this information, the element will follow the appropriate integration procedure (see Fig. 1b). Level set methods are for instance well suited for this purpose. We present below an alternative to the level set method which offers some advantages for the representation of complex crack networks.

We firstly define an edge status variable  $\mu$  for each edge with global index  $j$ :

$$\mu(j) = \begin{cases} -1, & \text{if no discontinuity at edge } E_j; \\ 0, & \text{if } E_j \text{ is at a crack tip;} \\ 1, & \text{if a crack crosses through } E_j. \end{cases} \quad (24)$$

and then define a dataset for each edge  $j$ :

$$\mu(j), \quad \xi(j) \quad (25)$$

where  $\xi(j)$  contains the natural coordinates of the intersection of a discontinuity with edge  $j$ , if such intersection exists. The dataset is then made available to all elements that include edge  $j$ . The initial status of a discontinuity (prior to an analysis) can be defined through an array of initial values for the dataset in Eq. 25.

### 3.6 Representation of a crack tip

Considering Fig. 2j, suppose that the strong discontinuity terminates at edge  $E_2$ , i.e., the element to the right of  $E_2$  has not failed. The existence of a crack tip at edge  $E_2$  implies that  $\mathbf{q}_6 = \mathbf{q}_{10}$ . Closing the crack tip can be achieved through internal assembly of floating nodes or using constraint equations.

Considering Figs. 3a and 3b, it is clear that closing the crack tip is not sufficient for an accurate representation of the crack tip; in fact; the transition from a strong discontinuity to no discontinuity can lead to an artefact whereby the element at the crack tip (see Figs. 3a and 3b) does not have the adequate topology for connecting to the adjacent uncracked element (lack of compatibility). Figs. 3c and 3d show that this can be mitigated to an extent using constraint equations which define the DoF at the crack tip through interpolation of suitable DoF of the element at the crack tip.

A better solution is shown in Figs. 3e and 3f; the lack of compatibility can be avoided by using a transition element at the crack tip (in fact, the code required for doing this is exactly the same that is used to represent weak discontinuities within the FNM).

Fig. 3g shows that refinement elements can be used as well, leading to further improvements in the representation of the crack tip. If at least one refinement element is used (Fig. 3g), then the one step virtual crack closure technique (VCCT) can be used directly to model propagation of strong discontinuities, as detailed in § 3.7.2.

## 3.7 Propagation of discontinuities

### 3.7.1 Stress based criteria with cohesive formulations

When a crack in a floating node element is represented through a cohesive model, with the lat-

ter having a stress-based failure initiation criterion embedded in its formulation, it is natural to also use an identical stress-based failure criterion to decide on the eventual propagation of a crack through an element. If the failure criterion for the cohesive element is:

$$f(\boldsymbol{\sigma}) = 0, \quad (26)$$

then the propagation criterion (to activate the floating DoF so as to form a cohesive sub-element along the potential crack path) can be:

$$f(\boldsymbol{\sigma}) = \epsilon, \quad \text{with } -1 \leq \epsilon \leq 0, \quad (27)$$

where  $\epsilon$  is a user-defined non-positive number such that the floating DoF are activated before propagation is due to occur.

### 3.7.2 Virtual crack closure technique

It is possible to propagate cracks without using stress measures directly; i.e. using fracture mechanics concepts only. For this, Virtual Crack Closure Technique (VCCT) [8] is particularly well suited for using with the FNM.

Consider Fig. 3g, where the element at the crack tip (refinement element labelled R) has not failed yet, but contains a weak discontinuity. The weak discontinuity is introduced to better represent the crack tip. It is equivalent to a local mesh refinement, and can be extended to several elements ahead of the crack tip. Let  $\mathbf{F}$  be the internal force vector at the crack tip and  $[[\mathbf{q}]]$  be the displacement jump at the opposing edge in the wake element. Also, let  $A_W$  be the area of the crack surface in the element on the wake of the crack (for a 2 dimensional problem,  $A_W = \ell_W b$ , where  $\ell_W$  is indicated in Fig. 3g and  $b$  is the thickness) and  $A_{CT}$  be the area of the crack surface in the element at the crack tip (for a 2 dimensional problem,  $A_{CT} = \ell_{CT} b$ , where  $\ell_{CT}$  is indicated in Fig. 3g). Then, the energy release rates for modes I and II can be calculated as [9]:

$$G_I = \frac{1}{2A_W} F_n [[q_n]] \left( \frac{A_W}{A_{CT}} \right)^{1/2} \quad (28)$$

$$G_{II} = \frac{1}{2A_W} F_t [[q_t]] \left( \frac{A_W}{A_{CT}} \right)^{1/2} \quad (29)$$

where  $F_n$  and  $F_t$  are, respectively, the components of  $\mathbf{F}$  in the normal and tangential directions to the crack, and  $[[q_n]]$  and  $[[q_t]]$  are respectively the

components of  $\llbracket \mathbf{q} \rrbracket$  in the normal and tangential directions to the crack.

Once the energy release rates are known, a criterion of the form:

$$f(G_I, G_{II}) = 0 \quad (30)$$

can be used to decide on the eventual propagation of a crack through the element and on the direction of the crack.

Calculating the energy release rates in Eqs. 28 and 29 requires that the element at a crack tip has access to the displacement jump at the opposing edge in the element in the wake of the crack. This can be achieved by expanding the dataset for each edge  $j$  (Eq. 25) with more information to become:

$$\mu(j), \quad \xi(j), \quad \llbracket \mathbf{q} \rrbracket(\bar{j}), \quad \mathbf{n}(\bar{j}), \quad A(\bar{j}) \quad (31)$$

where  $\llbracket \mathbf{q} \rrbracket(\bar{j})$  is the displacement jump at the other (opposing) edge of the element in the wake of the crack (W in Fig. 3g),  $\mathbf{n}(\bar{j})$  is the normal to the crack direction in element W, and  $A(\bar{j})$  is the crack area in element W.

### 3.8 Implementation in existing FE codes

The validation and application examples below were obtained through an implementation of the FNM in an User Element (UEL) subroutine in the commercial code Abaqus [10].

## 4 Validation

### 4.1 Convergence and accuracy

We compare the mesh convergence of the PNM and FNM in the evaluation of stress intensity factors (SIF) for an edge crack propagating in mode I (Fig. 4a). The numerical evaluations for the FNM are performed with VCCT as presented in § 3.7.2, and for PNM with VCCT as implemented in the commercial software Abaqus [10]. The model has dimensions  $W = 9$  mm,  $L = 37$  mm and  $a = 3$  mm. The Young's modulus is  $E = 200$  GPa and the Poisson's ratio is  $\nu = 0.3$ . The applied stress is  $\sigma = 1$  MPa. The plate is discretised uniformly

with  $n_W$  and  $n_L$  four-noded plane stress elements, in the width and height directions, respectively. The four meshes created have  $(n_W, n_L) = (9, 37); (18, 75); (36, 149)$  and  $(42, 173)$ . The results are summarized in Fig. 4b. The FNM can be seen to converge monotonically and more rapidly than the PNM used for comparison.

We now evaluate the stress intensity factors (SIF) for a centre slant crack (Fig. 5a) obtained by the FNM against the corresponding analytical solutions [11] in mode I ( $K_I$ ) and mode II ( $K_{II}$ ), for different orientations  $\theta$  of the crack. The numerical evaluations for the FNM are performed with VCCT as presented in § 3.7.2. For FNM with VCCT, when the crack separates the original element domain into a triangle and a pentagon, both the partitions shown in Fig. 2d and that shown in Fig. 2e are employed. The model has dimensions  $L = W = 10$  mm and the horizontal projection of the crack is  $a \cos \theta = 0.1W$ . The Young's modulus is  $E = 200$  GPa and the Poisson's ratio is  $\nu = 0.3$ . The applied stress is  $\sigma = 1$  MPa. The plate is discretised uniformly with a coarse mesh (80 elements across the width and 81 elements across the height). Plane stress conditions are assumed. The results are summarized in Fig. 5b. The data-points labelled 'Int. 1' are obtained with FNM-VCCT using the partition in Fig. 2d, and the data-points labelled 'Int. 2' are obtained with FNM-VCCT using the partition in Fig. 2e.

### 4.2 Crack propagation

A double cantilever beam (DCB) test is used to simulate a propagating crack for a case in which the analytical solution (using corrected beam theory [12]) is known. The material is representative of carbon/PEEK fibre reinforced composite [13] and is modelled as an orthotropic material. The geometry, boundary conditions and mesh are described in Fig. 6a; the width of the specimen is 25.4 mm; the elements are 0.25 mm in length and the most refined elements near the mid-section are 0.124 mm in height. The cohesive zone approach with a standard bi-linear law and a stress-based criterion as described in § 3.7.1 is employed to determine the initiation and propagation of a crack. Since the loading is purely in Mode I, the choice of failure initiation criterion and mixed-mode dam-



age propagation law are irrelevant; we therefore use the typical quadratic interaction criteria for both initiation and propagation.

This case is analysed with both the FNM and the PNM (the latter implemented in the commercial software Abaqus [10]). For the FNM, the transition element shown in Fig. 3f is employed for the element in front of the crack tip. The partitioning of the transition element into a floating node element containing a cohesive sub-element (Fig. 2i) is carried out as detailed in § 3.7.1 with  $\epsilon = 0$ . The propagation of the crack is then determined by the failure of the cohesive elements. The results are shown in Fig. 6b.

## 5 Application: modelling of the growth of matrix crack density in a cross-ply laminate

In this section, we analyse the problem of interaction between matrix cracks and delamination on a cross-ply  $[0_2/90_4]_S$  laminate of toughened glass/epoxy, tested in tension by Joffe and Varna [14]. In this problem, correctly capturing the matrix crack/delamination interaction mechanism is important for the accurate prediction of matrix crack saturation and consequent transition to delamination.

Fang et al. [15] (see Fig. 7a) showed that using non-matching meshes at a crack intersection (e.g. using the PNM for the  $90^\circ$  matrix cracks in the  $90^\circ$  ply and cohesive elements at the interface for the delamination) leads to an inaccurate representation of the displacement jump (and hence of the cohesive traction) at the interface. Capturing correctly the displacement jump requires further DoF at the intersection between cracks (Fig. 7b); the FNM method is particularly well suited to model intersecting cracks, capturing correctly the displacement jump at the interface.

Based on the FNM, an element specifically designed for cross-ply laminates is formed with both real nodes and floating nodes, as shown in Fig. 7c. It makes use of the known position of the interface, so that the interface is not seeded with real nodes (Fig. 7d); instead, it is represented by cohesive elements formed with floating nodes. In this way, minimum seeding is required during preprocessing.

Failure occurs essentially under tension (mode I) in the  $90^\circ$  ply and under shear (mode II) for the delamination. The choice of failure initiation criterion and mixed-mode damage propagation law are therefore largely irrelevant in this case. We therefore use the typical quadratic interaction criteria for both initiation and propagation. All material properties are taken from the literature [14, 16, 17]. Since the loading is uniform in tension, a 10% reduction on transverse tensile strength and mode I critical energy release rate is introduced in the element at the centre so as to initiate failure at the centre of the model. The model, Fig. 8a, represents half of the laminate, with symmetric boundary conditions applied on the bottom surface of the  $90^\circ$  plies.

Figs. 8b and 8c show the failure pattern predictions for the laminate when using the FNM element from Figs. 7c and 7d. To demonstrate how crucial it is to have matching meshes at the crack intersections, a second model was created, differing only in that only one cohesive sub-element is used to model the delamination in each FNM element (as in Fig. 7a), rather than two. This second model corresponds very closely to a model in which matrix cracks in the  $90^\circ$  ply are modelled with the PNM and the delamination is modelled independently using cohesive elements. The resulting crack pattern, at the same level of strain as in Figs. 8b and 8c, is shown in Figs. 8d and 8e. The second model predicts significantly less delamination than the FNM model. The simulation shows that delamination does not start from the element containing the matrix crack; instead, it occurs firstly in the elements next to the cracked element. This non-physical sequence of delamination propagation is expected in the formulation of the non-matching meshes (Fig. 7a).

Fig. 9 shows the crack density vs. applied strain predictions. While both models are able to capture the growth of crack density with applied strain, only the first model (with matching mesh at the crack intersections) is able to predict saturation accurately; the second model continues to predict an increase in crack density, albeit at a lower growth rate, after saturation should have occurred. This example thus demonstrates the capability of using the FNM to construct elements for the modelling of specific geometries and complex crack networks.

## 6 Conclusion

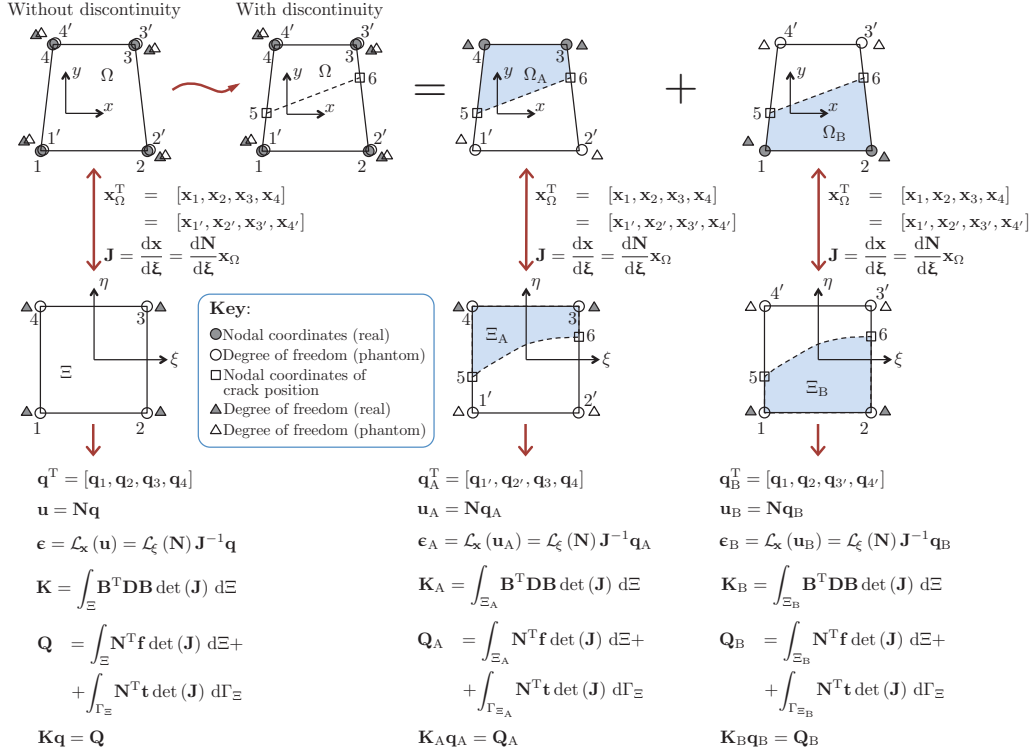
This paper proposes a floating node method which can be implemented in existing finite element packages. The paper demonstrates that the floating node method has the following advantages over alternative methods, in particular the phantom node method: (i) it does not introduce an error on the crack geometry when mapping from physical to natural coordinates; (ii) the integration is simple, as it does not require numerical integration over *only part* of a domain; (iii) it leads to the same solution as a finite element mesh where the discontinuity is represented explicitly; (iv) it can incorporate weak discontinuities and cohesive cracks readily; (v) it can be readily combined with VCCT; (vi) it provides accurate predictions for stress intensity factors under generic mode ratios; (vii) it is ideally suited for the representation of multiple and complex networks of (weak, strong and cohesive) discontinuities; and (viii) it can successfully predict certain interactions between matrix cracking and delamination.

## Acknowledgement

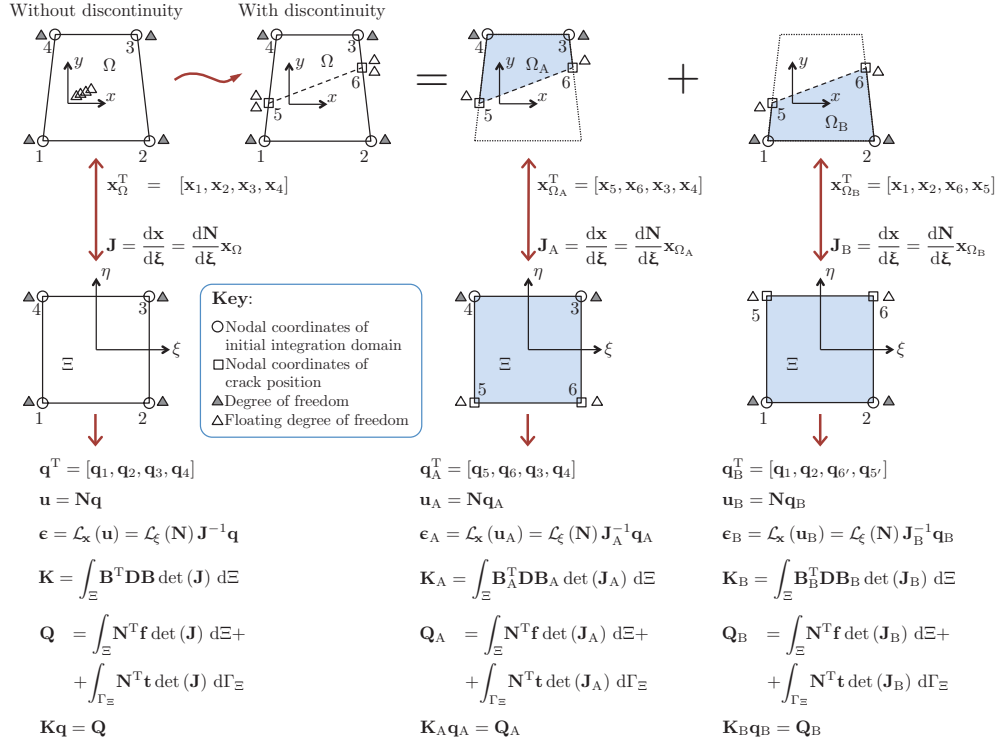
The second author acknowledges the scholarship from National University of Singapore.

## References

- [1] H. Azadi and A. R. Khoei, “Numerical simulation of multiple crack growth in brittle materials with adaptive remeshing,” *International Journal for Numerical Methods in Engineering*, vol. 85, pp. 1017–1048, 2011.
- [2] Z. P. Bažant and B. Oh, “Crack band theory for fracture of concrete,” *Matériaux et Construction*, vol. 16, no. 3, pp. 155–177, 1983.
- [3] S. T. Pinho, L. Iannucci, and P. Robinson, “Physically based failure models and criteria for laminated fibre-reinforced composites with emphasis on fibre kinking. Part II: FE implementation,” *Composites Part A-Applied Science and Manufacturing*, vol. 37, no. 5, pp. 766–777, 2006.
- [4] N. Moës, J. Dolbow, and T. Belytschko, “A finite element method for crack growth without remeshing,” *International Journal for Numerical Methods in Engineering*, vol. 46, no. 1, pp. 131–150, 1999.
- [5] J. J. C. Remmers, R. de Borst, and A. Needleman, “The simulation of dynamic crack propagation using the cohesive segments method,” *Journal of the Mechanics and Physics of Solids*, vol. 56, no. 1, pp. 70–92, 2008.
- [6] L. F. Kawashita, A. Bedos, and S. R. Hallett, “Modelling Mesh Independent Transverse Cracks in Laminated Composites with a Simplified Cohesive Segment Method,” *Computers, Materials & Continua*, vol. 32, no. 2, pp. 133–158, 2012.
- [7] P. M. A. Areias, J. H. Song, and T. Belytschko, “Analysis of fracture in thin shells by overlapping paired elements,” *Computer Methods in Applied Mechanics and Engineering*, vol. 195, no. 41–43, pp. 5343–5360, 2006.
- [8] E. F. Rybicki and M. F. Kanninen, “A finite element calculation of stress intensity factors by a modified crack closure integral,” *Engineering Fracture Mechanics*, vol. 9, no. 9, pp. 931–938, 1977.
- [9] R. Krueger, “Virtual crack closure technique: history, approach and applications,” *Applied Mechanics Reviews*, vol. 57, pp. 109–143, 2004.
- [10] Dassault Systèmes Simulia Corp., *Abaqus 6.10 documentation*. Providence, RI, USA: Dassault Systèmes, 2010.
- [11] H. Tada, P. C. Paris, and G. R. Irwin, *The stress analysis of cracks handbook*. Second edition, Paris Productions Incorporated (and Del Research Corporation), 226 Woodbourne Dr. St. Louis, Missouri, 1985.
- [12] J. R. Reeder, K. Demarco, and K. S. Whitley, “The use of doubler reinforcement in delamination toughness testing,” *Composites Part A: Applied Science and Manufacturing*, vol. 35, no. 11, pp. 1337 – 1344, 2004.
- [13] F. P. van der Meer and L. J. Sluys, “A phantom node formulation with mixed mode cohesive law for splitting in laminates,” *International Journal of Fracture*, vol. 158, no. 2, pp. 107–124, 2009.
- [14] R. Joffe and J. Varna, “Analytical modeling of stiffness reduction in symmetric and balanced laminates due to cracks in 90° layers,” *Composites Science and Technology*, vol. 59, no. 11, pp. 1641 – 1652, 1999.
- [15] X. J. Fang, Q. D. Yang, B. N. Cox, and Z. Q. Zhou, “An augmented cohesive zone element for arbitrary crack coalescence and bifurcation in heterogeneous materials,” *International Journal for Numerical Methods in Engineering*, vol. 88, pp. 841–861, 2011.
- [16] R. Joffe, A. Krasnikovs, and J. Varna, “COD-based simulation of transverse cracking and stiffness reduction in [S/90n]s laminates,” *Composites Science and Technology*, vol. 61, no. 5, pp. 637 – 656, 2001.
- [17] S. R. Hallett and M. R. Wisnom, “Numerical investigation of progressive damage and the effect of layup in notched tensile tests,” *Journal of Composite Materials*, vol. 40, no. 14, pp. 1229–1245, 2006.



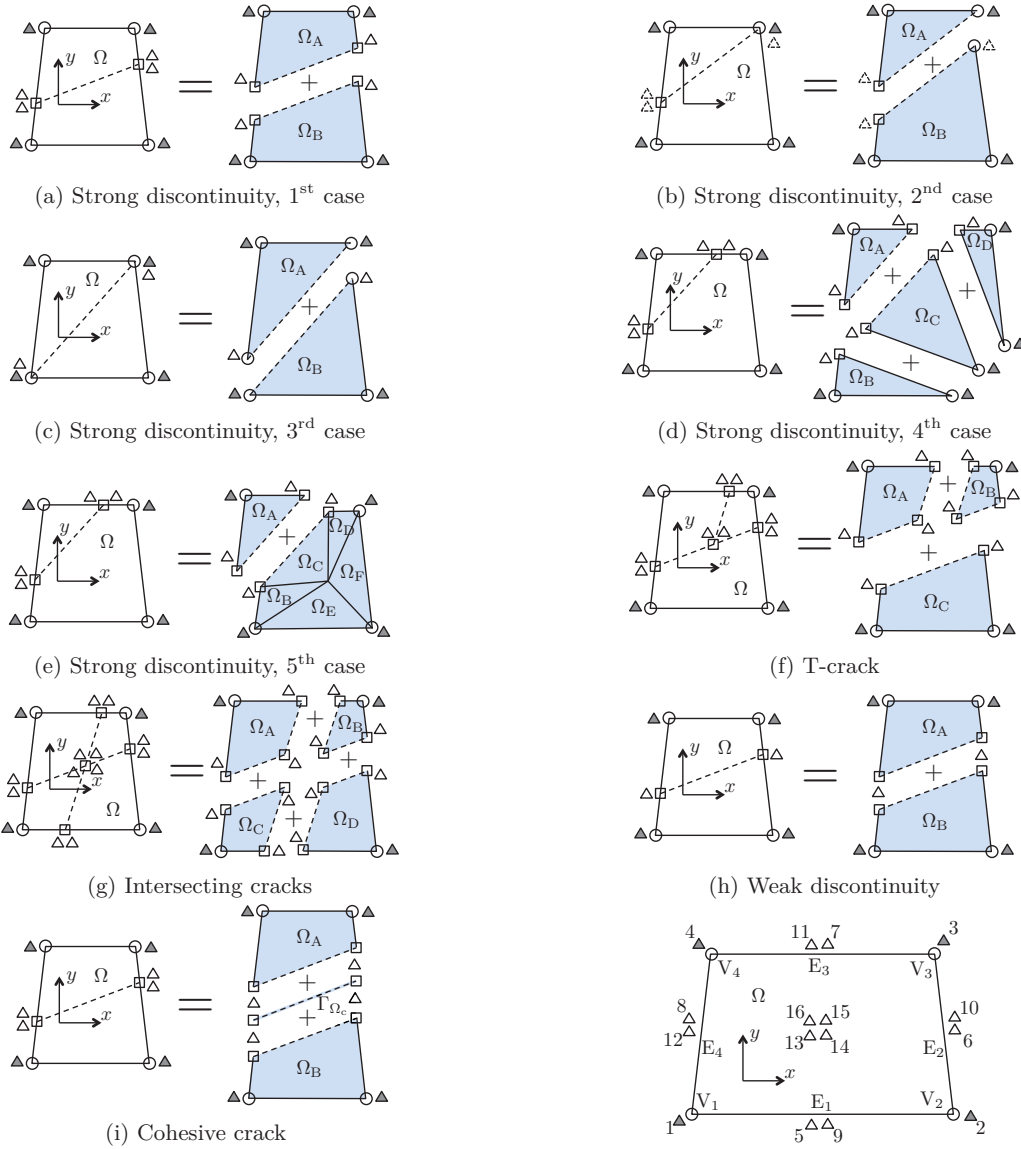
(a) Phantom Node Method



(b) Floating Node Method

Fig. 1. Comparison between the Phantom Node Method and the Floating Node Method.





(j) Example of local DoF, vertices and edges numbering for the floating node element in Fig. 2g. To facilitate assembly, a pair of floating DoF are associated with each edge, and four floating DoF are internal.

Fig. 2. Examples of different discontinuities that can be modelled by the Floating Node Method (see key in Fig. 1b).

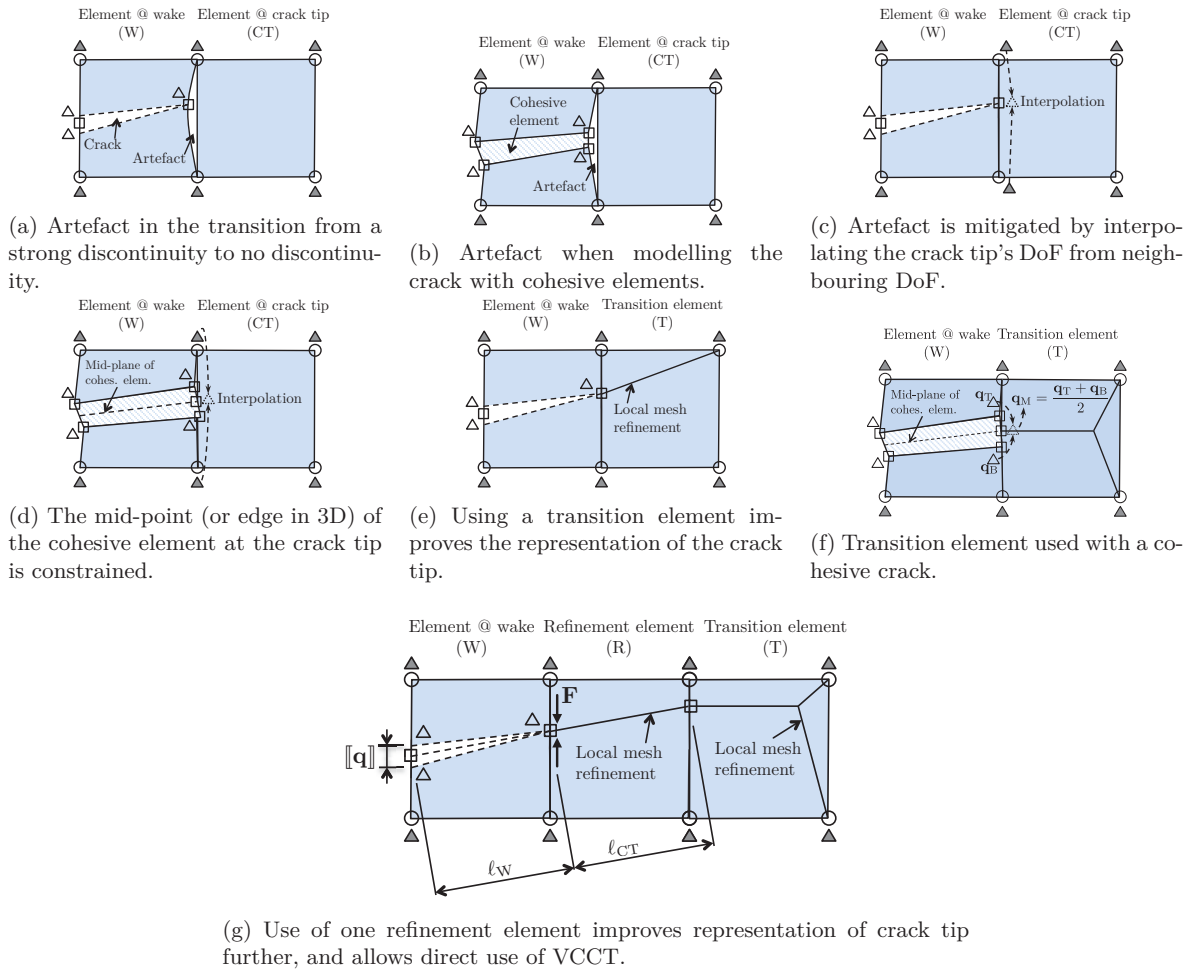


Fig. 3. Using local refinement elements and transition elements to represent the crack tip more accurately (see key in Fig. 1b).

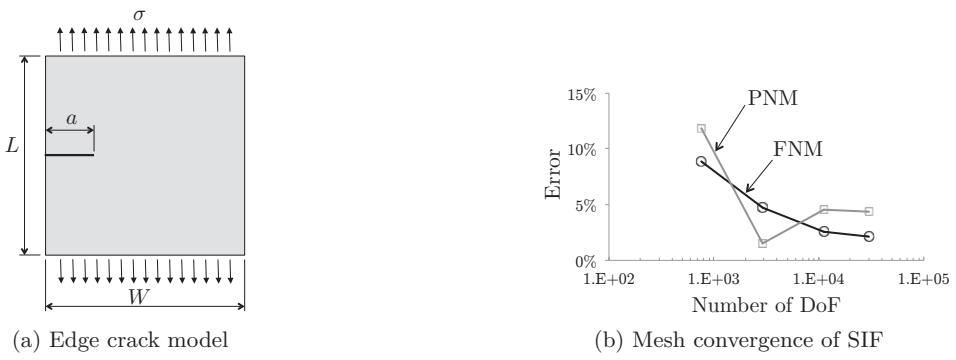


Fig. 4. For this edge crack model, the FNM converges monotonically, unlike the PNM.

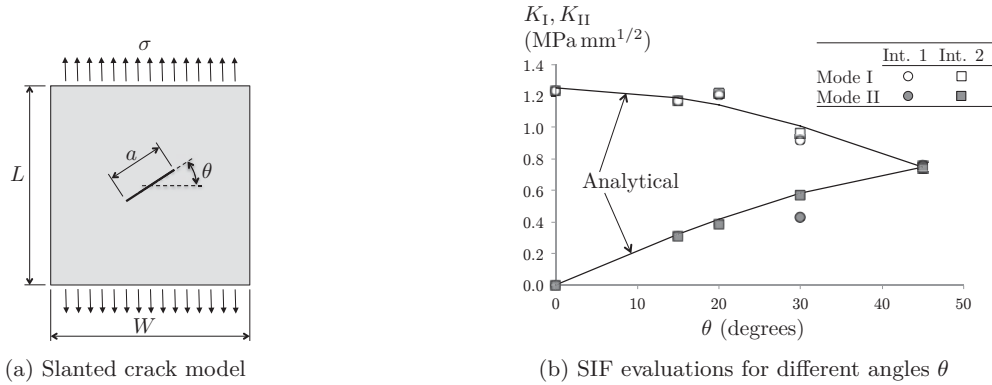


Fig. 5. For this slant crack model, the FNM captures the SIF well in modes I and II for different angles  $\theta$ .

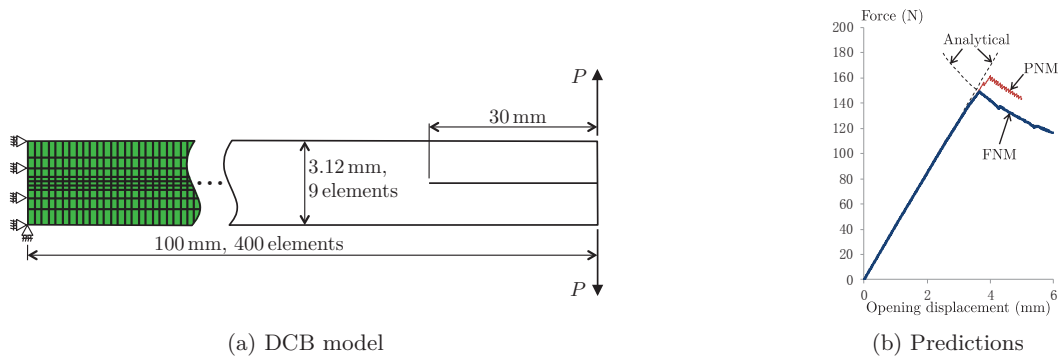


Fig. 6. DCB validation case, showing that, for the same mesh seeding, the FNM predicts accurately the force ( $P$ ) vs. displacement curve while the PNM overpredicts the force.

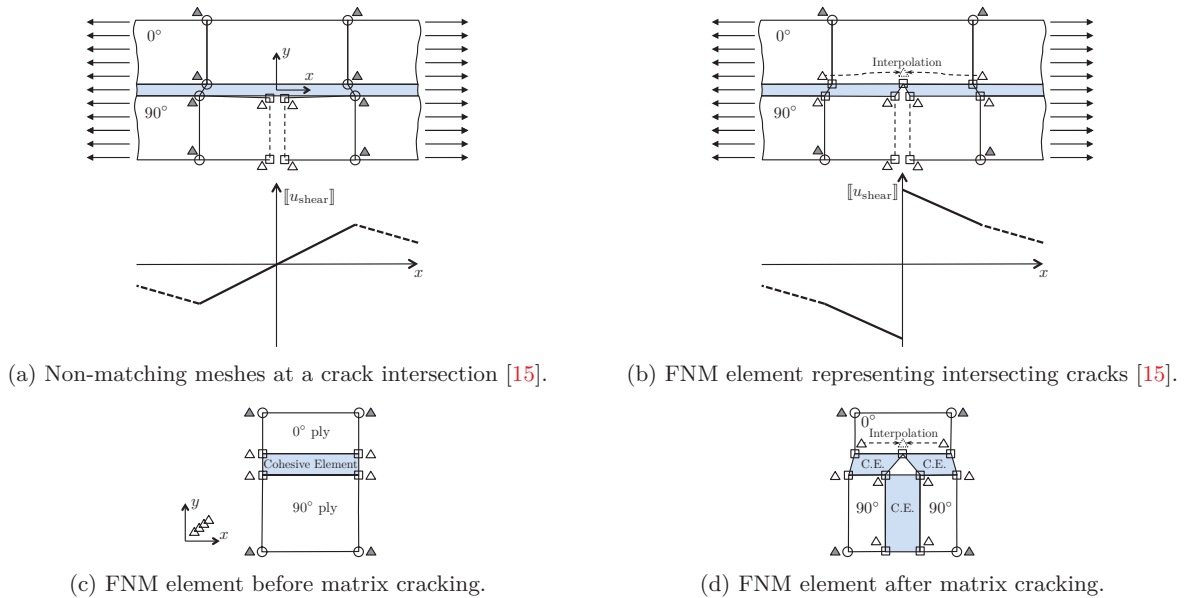
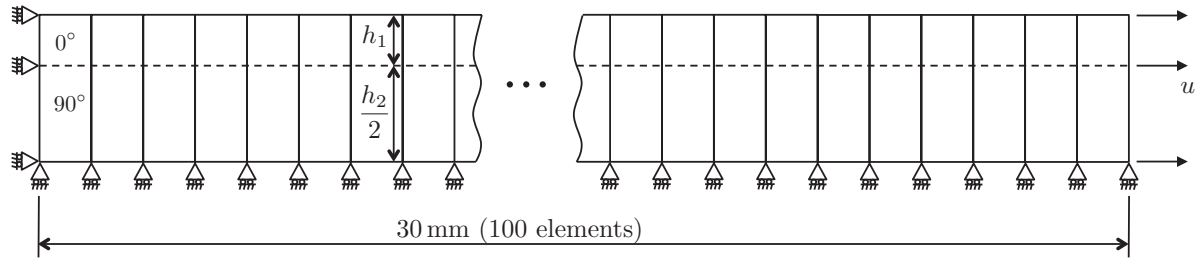


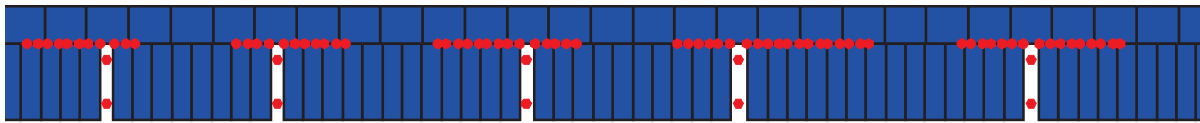
Fig. 7. Modelling the intersection between matrix cracks and delamination with non-matching meshes fails to capture the displacement jump; the FNM can address this.



(a) FNM model. Note that there is only one floating node element along the height (see Figs. 7c and 7d).



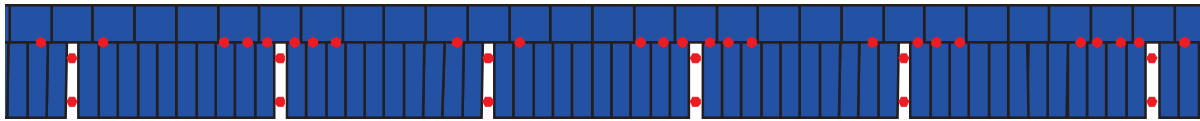
(b) Accurate modelling of the transition from matrix cracking to delamination when using the FNM element from Figs. 7c and 7d.



(c) Zoom of FNM mesh in Fig. 8b.



(d) Model with non-matching mesh at the intersection, showing that some transition to delamination is not correctly captured.



(e) Zoom of non-matching mesh in Fig. 8d.

Fig. 8. Modelling the transition from matrix cracking to delamination in a cross-ply composite specimen. The red dots indicate failure at the corresponding integration points.

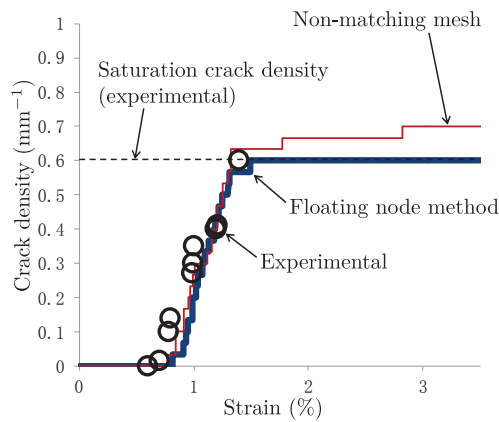


Fig. 9. The saturation crack density is correctly captured using the FNM element from Figs. 7c and 7d. Non-matching mesh results in over-prediction of this density. Experimental data is from Joffe and Varna [14].